THE JOURNAL OF PHYSICAL CHEMISTRY C

Article

pubs.acs.org/JPCC

Well-Organized Mesoporous TiO_2 Photoanode by Using Amphiphilic Graft Copolymer for Efficient Perovskite Solar Cells

Chih-Chun Chung,[†,‡] Chang Soo Lee,[‡,§] Efat Jokar,[†] Jong Hak Kim,[*,§] and Eric Wei-Guang Diau[*,†]

[†]Department of Applied Chemistry and Institute of Molecular Science, National Chiao Tung University, No. 1001, Ta-Hsueh Road, Hsinchu 30010, Taiwan

[§]Department of Chemical and Biomolecular Engineering, Yonsei University, 262 Seongsanno, Seodaemun-gu, Seoul 120-749, South Korea

Supporting Information

ABSTRACT: The control of the thickness and porosity of a mesoporous TiO_2 layer is important to improve the photovoltaic performance of perovskite solar cells. We produced organized mesoporous TiO_2 (om-TiO_2) layers using a low-cost amphiphilic graft copolymer, poly(vinyl chloride)-*graft*-poly(oxyethylene methacrylate) (PVC-*g*-POEM), as a sacrificial template. This simple but effective synthetic approach generates highly mesoporous and well-organized TiO_2 nanostructures with interconnected and size-tunable features. Specifically, the average pore size increased with the amount of hydrophobic PVC main chain in the graft copolymer, which acted as the pore forming agent. Perovskite layers were prepared on top of an om-TiO_2 layer according to a two-step sequential deposition: after coating the PbI_2 solution in dimethylformamide (DMF) on an om-TiO_2 substrate, the substrate was prewetted in isopropyl alcohol (IPA) solvent before immersing into a CH_3NH_3I/IPA solution. This prewetting treatment not only improves the yields of conversion from PbI_2 to $CH_3NH_3PbI_3$, but also increases the size of perovskite crystals with cuboid morphology. On varying the pore size and the film thickness of the om-TiO_2 layer, the device performance attained 11.9% of power conversion efficiency (PCE) at pore size 70 nm and film thickness 300 nm. We measured extracted charge densities and decays of transient photovoltage to understand the kinetics of charge recombination in relation to the corresponding device performance.

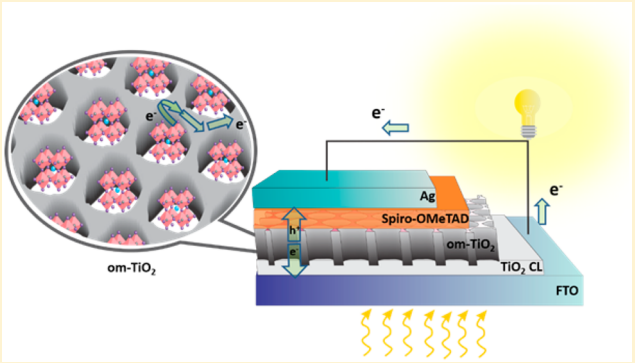

INTRODUCTION

All solid-state perovskite solar cells (PSC) have developed rapidly to achieve power conversion efficiency (PCE) over 20%.[1,2] Perovskite exhibits superior properties in both charge transport and light harvesting.[3−6] The architecture of PSC that dictates the choice of materials and fabrication plays a key role in the photovoltaic performance of the devices.[7−9] Planar[7] and mesoscopic[10,11] architectures are two common configurations for the fabrication of PSC. A typical mesoscopic structure of PSC contains a meso-structured photoanode, perovskite light-harvesting layer and hole-transporting material (HTM) layer. The mesoporous TiO_2 acts as a scaffold layer for the growth of perovskite crystals; it can act also as a layer to facilitate selective charge collection and suppression of charge recombination.[8] The morphology,[12] thickness,[13−15] and crystallinity[16] of the TiO_2 layer thus play a crucial role to determine the device performance for mesoscopic perovskite solar cells.

Various TiO_2 nanostructures have been developed as an efficient photoanode for PSC, such as TiO_2 nanoparticles,[17−20] aligned nanowires of TiO_2,[21,22] nanospherical aggregates of TiO_2,[23,24] and well organized mesoporous TiO_2.[25] Screen printing of a paste containing TiO_2 nanostructures is an ordinary method to prepare a uniform TiO_2 mesoporous film free of cracks. These TiO_2 pastes commonly contain particles of size 20−50 nm; the resulting films form a three-dimensional mesoporous network, but the preparation of the pastes is highly complicated and tedious. Moreover, because the random orientation of the nanoparticles in these films results in defects at grain boundaries, the rate of charge transport is limited.[26] To improve the charge transport inside the perovskite and to decrease the charge recombination at the interfaces, interconnection of the TiO_2 grains into a one-dimensional framework is an effective strategy. As a result, vertically aligned nanorods,[27] nanowires,[22] nanotubes,[28] nanosphere,[24] and well-organized mesoporous TiO_2[25] have been utilized as a layer for electron transport for PSC.

With the continuous growth of interest in organized mesoporous structure, an amphiphilic copolymer as a sacrificing template was essential to construct the mesoporous scaffold due to selective interaction of metal oxide precursor with the

Received: February 26, 2016
Revised: April 15, 2016
Published: April 15, 2016

DOI: 10.1021/acs.jpcc.6b01980
J. Phys. Chem. C 2016, 120, 9619−9627

hydrophilic domain of copolymer.[29−34] An amphiphilic block copolymer, such as P123 and F127, consisting of hydrophilic poly(ethylene oxide) (PEO) and hydrophobic poly(propylene oxide) (PPO) domains, has been most widely used to achieve the organized mesoporous structure through a favorable interaction of precursor with hydrophilic domain of polymer micelles.[35−38] In particular, the construction of mesoporous TiO_2 film prepared with block copolymer template has proved to be one of the powerful methods to improve the performance of PSC.[25,39] Seok et al. reported that the PSC with mesoporous TiO_2 film (pore diameter = 10−15 nm) prepared using Pluronic F127 and 1,3,5-trimethylbenzene as the sacrificial template exhibited a comparable conversion efficiency with a conventional crystalline TiO_2 nanoparticle films.[25] Moreover, the mesoporous TiO_2 film with larger pores exhibited higher conversion efficiency due to the easier pore filling of perovskite. However, this approach has some disadvantages such as complicated process and high cost to synthesize the block copolymer templates and difficulty in obtaining larger pore sizes (in particular, above 50 nm). Thus, alternative copolymer template that can be easily synthesized and generate larger pores is highly demanded.

In the present work, we first report efficient PSC based on organized mesoporous TiO_2 (om-TiO_2) layers prepared using a low-cost amphiphilic graft copolymer, poly(vinyl chloride)-*graft*-poly(oxyethylene methacrylate) (PVC-*g*-POEM), as a sacrificial template. A uniform and interconnected om-TiO_2 layer was obtained on spin-coating solutions containing PVC-*g*-POEM graft copolymer and titanium tetraisopropoxide (TTIP) precursor in various proportions after calcination at 450 °C. A perovskite layer on the surface of om-TiO_2 was deposited with a sequential method. Prewetting the om-TiO_2/PbI_2 substrate with 2-propanol (IPA) served as an effective treatment to enhance the perovskite loading. Scanning electron microscope (SEM) images, X-ray diffraction (XRD) patterns and absorption spectra confirmed an effective conversion from PbI_2 to $MAPbI_3$ through this prewetting approach. Pore size 30−70 nm and film thickness 300−800 nm of the om-TiO_2 layer were investigated. The best performance of the om-TiO_2-based device shows PCE 11.9% at pore size 70 nm and film thickness 300 nm. We measured and analyzed decays of charge extraction and transient photovoltage to obtain the extracted charge densities and electron lifetimes interpretable for the corresponding device performance.

EXPERIMENTAL SECTION

Synthesis of PVC-*g*-POEM Graft Copolymer Template. First, 6 g of PVC (M_n ∼ 55000 g/mol, Sigma-Aldrich) was dissolved in 50 mL of *N*-methyl-2-pyrrolidone (NMP) at 70 °C for 3 h to prepare a homogeneous polymer solution. Then, 0.1 g of CuCl (Sigma-Aldrich), 0.24 mL of 1,1,4,7,10,10-hexamethyltriethylenetetramine (HMTETA, Sigma-Aldrich) and 9 g of POEM (POEM, M_n ∼ 500 g/mol, Sigma-Aldrich) were added to the PVC solution and purged with nitrogen for 30 min. The mixture was heated at 90 °C for 24 h and precipitated in excess methanol. The resulting polymer was further purified by dissolving it in tetrahydrofuran (THF) and by reprecipitation in methanol for several times. The PVC-*g*-POEM graft copolymer was dried at 50 °C overnight and further dried in vacuum oven at 50 °C for 24 h.

Synthesis and Device Fabrication. Dense TiO_2 in a layer of thickness 60 nm was deposited on fluorine-doped tin oxide (TEC7, Hartford, U.S.A.) via spin coating a mildly acidic solution of titanium(IV) isopropoxide (TTIP, Sigma-Aldrich) precursor in IPA solution. The om-TiO_2 layer was synthesized using the graft copolymer as a template, as reported elsewhere.[40] The thickness of om-TiO_2 was varied with the concentration of PVC-*g*-POEM in THF. Solutions of polymer at 2, 3 and 4% were used for the synthesis of om-TiO_2 with film thicknesses 300, 500, and 800 nm, respectively. A TTIP sol−gel solution was separately prepared on slowly dropping HCl and H_2O in TTIP (TTIP/HCl/H_2O = 2:1:1, volume ratio) under vigorous stirring. After 30 min, the TTIP sol−gel solutions (0.4, 0.6, and 0.8 mL) were added to the PVC-*g*-POEM solutions (2, 3, and 4%, respectively) and stirred for 4 h. The obtained solution was spin-coated on the TiO_2 as prepared in a layer at 1500 rpm and annealed at 450 °C for 30 min.

CH_3NH_3I (MAI) was synthesized as reported elsewhere.[11] A perovskite layer was deposited on an om-TiO_2 substrate with a sequential method[41] but with modification via a prewetting approach detailed as follows. Lead iodide (1.0 M, 99%, Aldrich) was dissolved in *N*,*N*-dimethylformamide (DMF, anhydrous, Aldrich) under stirring at 70 °C for 6 h. This PbI_2 solution was spin-coated onto om-TiO_2 at 6500 rpm for 90 s, followed with drying on a hot plate at 70 °C for 30 min. In a conventional sequential method, the PbI_2/TiO_2 substrate is immersed in MAI/IPA solution. In our approach, the PbI_2/om-TiO_2 substrate was wetted with IPA solvent first for 2 s; this substrate was then immersed in MAI/IPA solution (10 mg/mL) for 2 min. The sample was subsequently rinsed with IPA and dried at 70 °C for 30 min again. The sample was then deposited on the HTM layer with a solution containing spiro-OMeTAD (125 mg, Lumtec), Li-TFSI (7.8 mg, Aldrich) in acetonitrile (15.6 μL) and 4-*tert*-butylpyridine (TBP, 22.6 μL) dissolved in chlorobenzene (1 mL) via spin-coating at 2000 rpm for 30 s. The sample was transferred to a vacuum system (10^{-6} Torr) in which silver (thickness 150 nm) was evaporated to complete the device fabrication.

Characterization of Materials and Devices. Fourier transform infrared (FT-IR) spectra of monomers and graft copolymers were measured using Spectrum 100 (PerkinElmer). H^1 NMR (nuclear magnetic resonance, 600 MHz high-resolution, Bruker, Ettlingen, Germany) measurements were used to analyze the composition of graft copolymer. Thermogravimetric analysis (TGA) was conducted at a heating rate of 10 °C/min under nitrogen using TA Instruments (U.S.A.). A field-emission scanning electron microscope (FESEM, Hitachi SU8010) was used to investigate the morphology and structure of the samples. Powder X-ray diffraction (XRD) was performed with a X-ray diffractometer (Bruker AXS, D8 Advance, Cu Kα irradiation, λ = 154.18 pm). With a digital source meter (Keithley 2400) we recorded the current−voltage curves of the devices under one-sun illumination (AM 1.5G, 100 mW cm^{-2}) from a solar simulator (XES-40S1, SAN-E1) with a scan rate 1.82 V/s. The action spectra of efficiency of conversion of incident photons to current (IPCE) were measured with a system comprising a Xe lamp (A-1010, PTi, 150 W) and a monochromator (PTi). Absorption spectra were recorded with a spectrophotometer (JASCO V-570).

RESULTS AND DISCUSSION

Synthesis and Characterization of Graft Copolymer Template and om-TiO_2 Layer. The PVC-*g*-POEM graft copolymer was synthesized and used as a sacrificial template for the fabrication of om-TiO_2 layer, because graft copolymers are

DOI: 10.1021/acs.jpcc.6b01980
J. Phys. Chem. C 2016, 120, 9619−9627

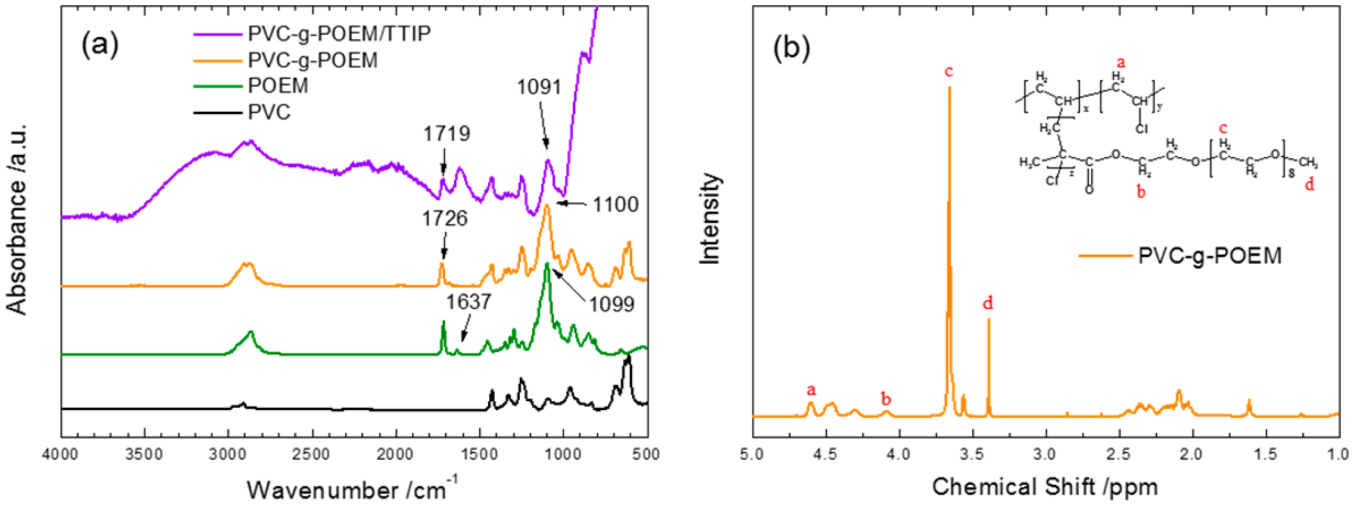

Figure 1. (a) FT-IR spectra of neat PVC, POEM macromonmer, PVC-*g*-POEM graft copolymer and PVC-*g*-POEM/TTIP hybrid before calcination and (b) H NMR spectrum of PVC-*g*-POEM graft copolymer.

more attractive than conventional block copolymers due to their lower cost and easier synthesis.[29−38] The synthesis is based on atom transfer radical polymerization (ATRP) by grafting the hydrophilic POEM side chain on the hydrophobic PVC backbone to provide the amphiphilic property. The PVC-*g*-POEM was combined with TTIP to form om-TiO_2 layer. The interactions of materials were characterized using FT-IR spectra, as shown in Figure 1a. The PVC-*g*-POEM graft copolymer exhibited the strong bands at 1726 and 1100 cm^{-1} due to the carbonyl (C═O) and ether (C−O−C) stretching modes, respectively, of POEM side chains, as well as the chloride (C−Cl) band of PVC main chain at 611 cm^{-1}.[40,42,43] Moreover, the alkene (C═C) stretching band at 1637 cm^{-1} of POEM completely disappeared in PVC-*g*-POEM, demonstrating that the PVC-*g*-POEM graft copolymer was successfully synthesized via ATRP reaction without any residual monomers. Upon combining PVC-*g*-POEM with TTIP before calcination, a broad strong absorption band was observed in the wavenumber region below 800 cm^{-1}, attributed to the Ti−O bonds in amorphous TiO_2. The carbonyl (C═O) band at 1726 cm^{-1} and ether (C−O−C) band at 1100 cm^{-1} of pristine PVC-*g*-POEM shifted to lower wavenumbers at 1719 and 1091 cm^{-1}, respectively, for PVC-*g*-POEM/TTIP hybrid. It might be due to the coordination interaction of TTIP with the hydrophilic POEM side chains, resulting in decreased bond strength by attracting the unoccupied electrons in oxygen, according to the Hooke's law:[44] $\nu = \frac{1}{2\pi c}\sqrt{\frac{k}{\mu}}$, where ν is vibrational frequency in wavenumber, k is a force constant, and μ is a reduced mass of molecules in chemical bonds.

As shown in Scheme 1, Ti^{4+} site in TTIP could be selectively combined with the unoccupied electrons in the ether (C−O−C) or carbonyl (C═O) group, resulting from the dipole−dipole interaction due to a higher electronegativity of oxygen (3.5) than carbon (2.5).[45] Therefore, to synthesize the organized structure of TiO_2, the amphiphilic property of PVC-*g*-POEM graft copolymer template is highly important to induce the coordination interaction and selective confinement of TTIP in the hydrophilic POEM domain. The H NMR spectrum was also employed to support the graft copolymerization and to determine the actual composition of PVC-*g*-POEM. The weight ratio between PVC main chains and

Scheme 1. Schematic Illustration for the Selective Interaction of TTIP with the POEM Side Chains of PVC-*g*-POEM Amphiphilic Graft Copolymer

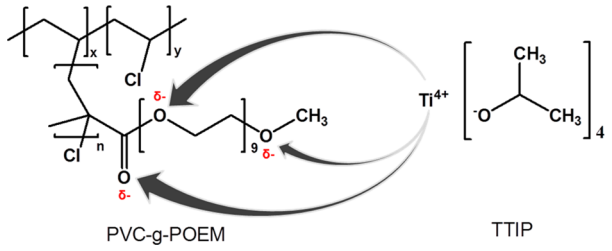

POEM side chains was calculated using the area of representative chemical shifts of PVC and POEM (Figure 1b). The PVC-*g*-POEM graft copolymer exhibited strong proton signals at δ = 4.60 and 3.66 ppm, which is attributed to the $-CH_2-$ group of PVC and $-CH_2CH_2O-$ group of POEM, respectively.[40,46] Using these signals, the actual weight ratio of PVC-*g*-POEM synthesized using PVC/POEM = 1:1.5 was determined to be approximately PVC/POEM = 4:1.

The TGA curves of PVC, POEM, PVC-*g*-POEM, and PVC-*g*-POEM/TTIP were obtained under N_2 as a function of temperature with constant ramping rate (10 °C/min), as shown in Figure 2a. The two-step thermal decomposition was observed for neat PVC with the onset decomposition point at 250 and 410 °C, respectively. The amount of first decomposition from 250 to 320 °C was approximately 62.0%, attributable to the weight loss of HCl as the stoichiometric content of HCl in PVC was approximately 58.4%. The residual hydrocarbons were thermally degraded during the second decomposition step from 420 to 550 °C. However, after the polymerization of POEM side chain, the PVC-*g*-POEM graft copolymer exhibited much steeper decomposition behavior in the temperature range between 350 and 450 °C, resulting from the removal of residue hydrocarbons in POEM side chains. Moreover, the onset point of first degradation temperature increased because the relative amount of unstable, reactive chlorine atom in PVC-*g*-POEM was reduced. When the PVC-*g*-POEM was combined with TTIP precursor, the thermal degradation behavior of PVC-*g*-POEM sacrificial template was similar to that of neat PVC, while approximately 44% of total

DOI: 10.1021/acs.jpcc.6b01980
J. Phys. Chem. C 2016, 120, 9619−9627

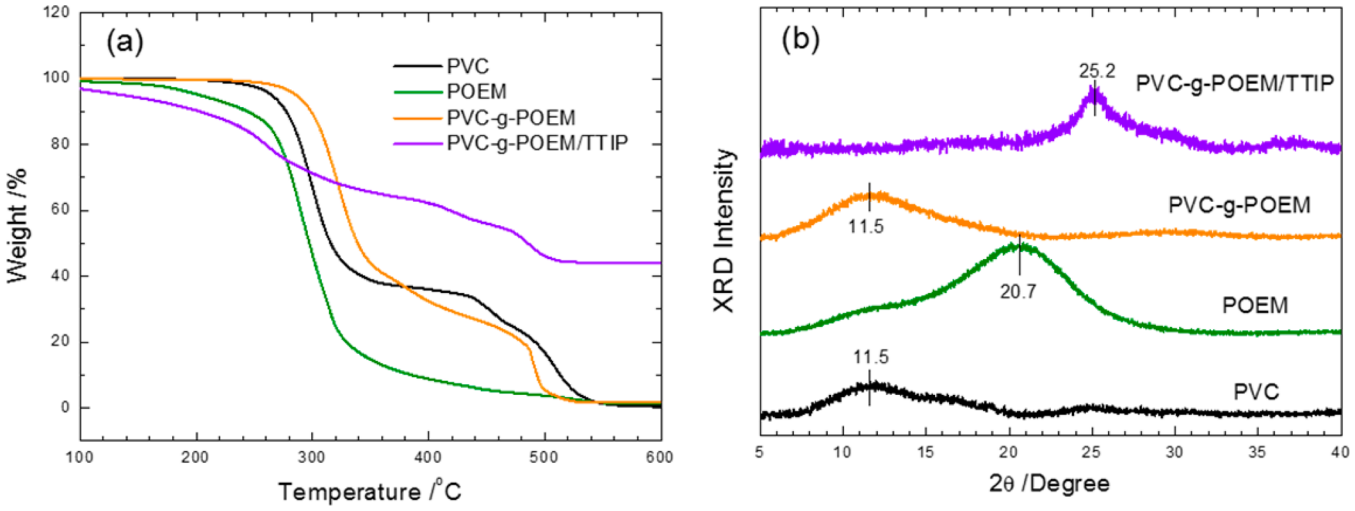

Figure 2. (a) TGA curve of PVC, POEM, PVC-*g*-POEM, and PVC-*g*-POEM/TTIP under N_2, (b) XRD patterns of PVC, POEM, PVC-*g*-POEM, and PVC-*g*-POEM/TTIP.

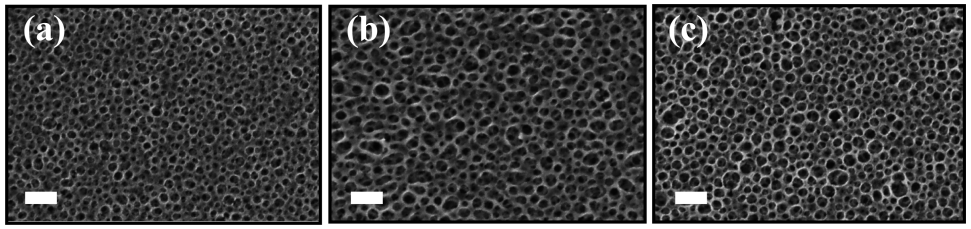

Figure 3. Top-view SEM images of an om-TiO_2 layer with pore sizes: (a) 30, (b) 50, and (c) 70 nm. Scale bars represent 100 nm for all images.

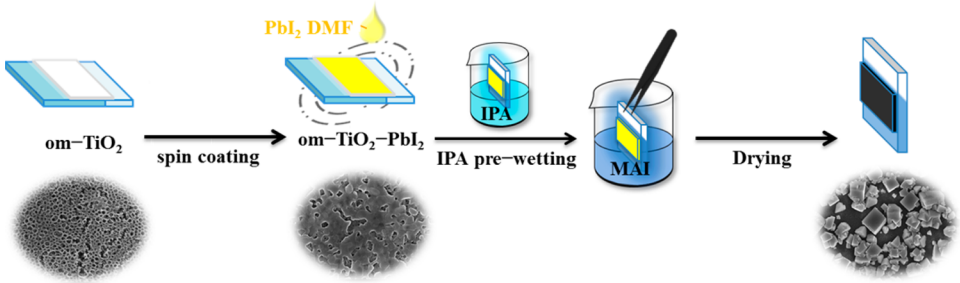

Figure 4. Schematic illustration of synthesis of the perovskite (PSK*) cuboid crystals on om-TiO_2 layer according to a sequential method with IPA prewetting treatment.

amounts was remained for PVC-*g*-POEM/TTIP due to the formation of crystalline TiO_2 (conversion yield ~ 44%). It should be noted that the om-TiO_2 layers were prepared using the calcination temperature of 450 °C, which is enough to degrade the PVC-*g*-POEM under O_2 (vs TGA obtained under N_2) to form crystalline anatase TiO_2 (which will be characterized later).

The structural properties of PVC, POEM, PVC-*g*-POEM, and PVC-*g*-POEM/TTIP were characterized using XRD spectra (Figure 2b). A broad diffraction pattern was observed for neat PVC and POEM macromonomer centered at 2θ values of 11.5 and 20.7°, respectively. It is attributed to the amorphous nature of PVC and POEM with a lack of crystallinity. Broad amorphous pattern indicates broadly distributed interchain *d*-spacing. Even after the graft polymerization of POEM side chains on PVC backbone, the amorphous structure of PVC was maintained at 2θ value of 11.5°. Moreover, the PVC-*g*-POEM/TTIP before calcination exhibited a relatively sharp diffraction peak at 2θ = 25.2° due to the formation of amorphous TiO_2.

The om-TiO_2 layers were prepared through a sol−gel process based on the hydrolysis and condensation of TTIP using PVC-*g*-POEM graft copolymer template.[40] The amphiphilic property of PVC-*g*-POEM induced a selective coordination of TTIP to the hydrophilic POEM domain while the uncoordinated hydrophobic PVC domain served as the pore forming agent to produce a mesoporous structure after calcination. This simple but effective approach causes a highly mesoporous structure with interconnected and size-tunable features of om-TiO_2: the pore size increased with an increasing amount of the PVC hydrophobic domain in the copolymer composition. Figure 3 shows top-view SEM images of om-TiO_2 layers with pore sizes 30, 50, and 70 nm; ordered and interconnected mesoporous structures with uniform pore size were clearly obtained. The organized mesoporous morphology with high porosity, large pore size, and good interconnectivity

DOI: 10.1021/acs.jpcc.6b01980
J. Phys. Chem. C 2016, 120, 9619−9627

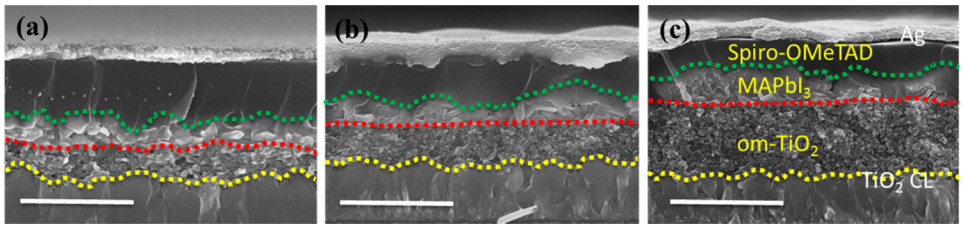

Figure 5. Side-view SEM images of devices made of om-TiO_2 with film thickness (a) 300, (b) 500, and (c) 800 nm. The yellow, red, and green dotted curves show the boundaries of a TiO_2 compact layer (CL), om-TiO_2 layer, and $MAPbI_3$ capping layer, respectively. Scale bars represent 1 μm for all images.

would be advantageous in terms of penetration of perovskite, large surface area to contact with perovskite and electron transport through the om-TiO_2 layer. Therefore, the PVC-*g*-POEM plays an essential role to fabricate the organized morphology of om-TiO_2, which, in turn, to enhance the overall efficiency of perovskite solar cells. It should be noted that the thickness of om-TiO_2 layer was easily controllable by varying the concentration of the PVC-*g*-POEM/TTIP solution. Moreover, the organized mesoporous morphology was not significantly perturbed depending on the thicknesses of om-TiO_2 layer, indicating the robust role of PVC-*g*-POEM as the sacrificial template.

Device Fabrication and Performances Characterization. Figure 4 shows the deposition scheme to generate a perovskite layer on top of the om-TiO_2 substrate according to a sequential approach with IPA prewetting treatment. According to the conventional method, the perovskite layer was deposited in two steps:[41] the om-TiO_2 substrate was covered with a PbI_2 layer with spin coating to produce the om-TiO_2/PbI_2 substrate; this substrate was then immersed in the MAI/IPA solution to form perovskite crystals (labeled PSK), but we found that insufficient perovskite was produced in this way, as judged from the brown color of the film shown in the picture of this device. We, hence, developed a prewetting procedure for the om-TiO_2/PbI_2 substrate that involved dipping it in IPA solvent for two seconds before the second immersion. This pretreatment wetted the surface of om-TiO_2/PbI_2, thereby enhancing the conversion of PbI_2 to form perovskite crystals (labeled PSK*) and increased the loading of perovskite on the surface of TiO_2. The PSK* device exhibits a color darker than that of the PSK device, because the perovskite film of the former is thicker than that of the latter, confirmed by the SEM images shown in Figure S1, Supporting Information (SI). Both PSK and PSK* show a cuboid crystal morphology produced on the surface of om-TiO_2, but the crystals of PSK* are significantly larger than those of PSK. We expect that the effect of prewetting on generating larger crystals was due to the formation of a thin IPA layer on the surface of om-TiO_2/PbI_2, so that the reaction of PbI_2 and MAI was significantly retarded. This retardation of crystal growth led to a formation of crystals larger for PSK* than for PSK, as observed in Figure S1, SI. Moreover, the prewetting of IPA increases the efficiency of conversion from PbI_2 and MAI to form $MAPbI_3$ as discussed in the following.

Figure S2a,b, SI, shows XRD patterns and absorption spectra, respectively, for PbI_2, PSK, and PSK* deposited on om-TiO_2 with pore size 70 nm and film thickness 500 nm. For the substrate with only PbI_2 on om-TiO_2 (the first step), the XRD patterns exhibit three signals characteristic of PbI_2 at 12.5, 38.5, and 52.1°, indicated with gray dotted lines in Figure S2a, SI. After immersion of the substrates in the MAI/IPA solution (the second step), the labeled signals in the range 14−50° represent the XRD patterns of perovskites (PSK and PSK*) in varied lattice planes of the tetragonal structure.[41,47] We found two major differences in the XRD patterns between PSK and PSK*: first, the patterns of PSK* show greater intensities than those of PSK, consistent with the larger crystal size of PSK* than that of PSK; second, the three residual PbI_2 signals highlighted in dotted lines show a much greater contribution in the PSK pattern than in the PSK* pattern, indicating that the conversion yield of PSK* with IPA prewetting was much greater than that of PSK without this prewetting. As the residual PbI_2 might induce a passivation effect to decrease the performance in perovskite solar cells,[48] decreasing the unreacted PbI_2 would be effective to improve the cell performance. The effect of prewetting was confirmed with the absorption spectra shown in Figure S2b, SI. The om-TiO_2/PbI_2 substrate shows characteristic absorption in the visible region (λ < 500 nm). The total absorbance of the PSK spectrum is larger than that of the PSK* spectrum in the region 400−600 nm, which is indicative of the residual PbI_2 contribution being larger for the former than for the latter.

The PSK and PSK* devices were fabricated according to the procedure shown in Figure 4, with additions of HTM and Ag back contact electrode detailed in the Experimental Section. The current−voltage curves and the action spectra of efficiency of conversion of incident photons to current (IPCE) of the devices made of PSK and PSK* are presented in Figure S3a and b, SI, respectively; the corresponding photovoltaic parameters are shown in Table S1, SI. The PSK* device demonstrates a short-circuit photocurrent density J_{SC} = 18.66 mA cm^{-2}, open-circuit voltage V_{OC} = 0.948 V and PCE = 9.8%, which is slightly greater than that of the PSK device without prewetting, 9.4%. For comparison, we also fabricated the mesoscopic perovskite device using the same sequential method but with conventional TiO_2 mesoporous layer (HD type, particle size ~50 nm).[49] The photovoltaic performance of the HD-based device (PCE = 8.4%) was significantly poorer than those of the om-TiO_2 devices (Table S1, SI). The shape of the IPCE spectra of these devices agrees satisfactorily with those reported elsewhere,[41] but much greater IPCE values were obtained to yield larger J_{SC} values for the om-TiO_2-based PSK* and PSK devices than for the HD-based device. This enhanced J_{SC} for the PSK* device might be due to the increased conversion yield from PbI_2 to $MAPbI_3$ that increased the amount of perovskite loading for the PSK* device with prewetting than for the PSK device without prewetting.

After the improved production of the perovskite layer due to prewetting in a sequential deposition, the om-TiO_2 structure was modified with a varied pore size. As Figure 3 shows, the pore sizes of om-TiO_2 are varied on modifying the hydrophobic domain of the graft copolymer. The current−voltage curves of the perovskite solar cells fabricated with om-TiO_2 structures of

DOI: 10.1021/acs.jpcc.6b01980
J. Phys. Chem. C 2016, 120, 9619−9627

varied pore size are shown in Figure S4, SI; the corresponding photovoltaic parameters are listed in Table S2, SI. To examine the effect of hysteresis for the $J-V$ scans, the potential was swept in both forward and backward directions for om-TiO_2 with film thickness 500 nm and pore size 70 nm. As the results shown in Figure S5, SI, only slight hysteresis was observed for this type of perovskite solar cells. For the photovoltaic effect on pore sizes, both the J_{SC} and V_{OC} values increased when the pore size of om-TiO_2 increased from 30 to 70 nm. The device made of om-TiO_2 with pore size 70 nm shows the best performance, PCE 9.8%. In our approach to prepare om-TiO_2 films, not only the pore size, but also the thickness of the mesoporous layer, was controlled on varying the concentration of the solution; om-TiO_2 of thickness 300, 500, and 800 nm was prepared accordingly. We thus fabricated PSK* devices with these om-TiO_2 layers with the same pore size, 70 nm; the corresponding side-view SEM images appear in Figure 5.

According to the device configurations shown in Figure 5, 15 devices were fabricated under the same experimental conditions for each film thickness of om-TiO_2; the corresponding photovoltaic parameters are summarized in Tables S3–5, SI. Figure 6 compares the performance distributions of these results with varied thickness of the om-TiO_2 layer, giving mean PCE /% = 11.0 ± 0.7, 9.2 ± 0.4, and 8.2 ± 0.5 for devices made of om-TiO_2 films at 300, 500, and 800 nm, respectively. It is worth noting that the film morphology of perovskite is an important factor to be considered to promote the device performance for perovskite solar cells. For example, solvent–induced crystallization[50−51] and additive methods[52−54] have been reported to improve the cell efficiency for planar heterojunction devices. For mesoscopic devices as reported herein, a sequential method was applied and the crystal morphology was difficult to control. As a result, the best efficiency reported in this study attaining only ∼12%. Based on our prewetting approach using the sequential method, the size of perovskite crystals on top of om-TiO_2 was increased to submicrometer scale but with random orientation (Figure S1, SI). We believe that the roughness of the perovskite film induces some negative effect that caused to a lower efficiency as we observed.

Figure 7a,b show the best photovoltaic performances and the corresponding IPCE spectra, respectively, for devices made of these three om-TiO_2 films. Like the photovoltaic parameters in Table 1, the data exhibit a systematic trend for both J_{SC} and V_{OC} that decreased with film thickness 300 nm increasing to 800 nm. The best performance occurred with the device made of om-TiO_2 of thickness 300 nm, PCE = 11.9%, which outperforms those films of 500 nm, PCE = 9.8%, and of 800 nm, PCE = 8.9%.[55] The trend of J_{SC} in this series reflects the

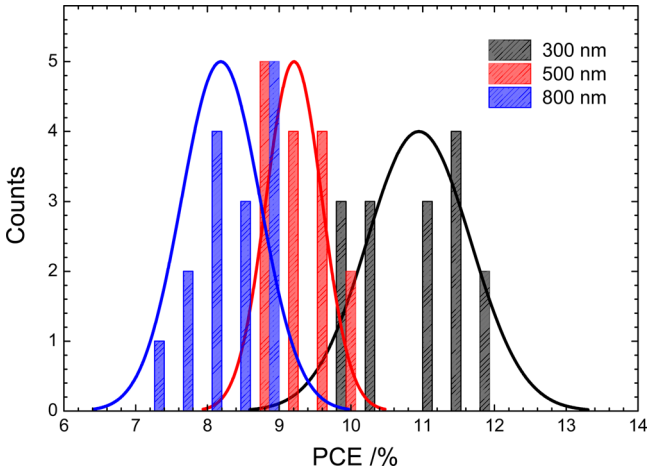

Figure 6. Histogram of PCE showing performance distributions of PSK* devices with om-TiO_2 of film thickness 300, 500, and 800 nm, fabricated under the same experimental conditions.

Table 1. Photovoltaic Parameters of Meso-Structured Perovskite Solar Cells (PSK*) Fabricated with Pore Size 70 nm and Varied Thickness of om-TiO_2 Layer under Simulated AM-1.5G Illumination (Power Density 100 mW cm^{-2}) with Active Area 0.09 cm^2 and Scan Rate 1.8 V/s[a]

om-TiO_2 thickness (nm)	J_{SC} (mA cm^{-2})	integrated current (mA cm^{-2})	V_{OC} (mV)	FF	PCE (%)
300	20.21	17.09	982	0.599	11.9 (11.0 ± 0.7)
500	18.71	15.59	947	0.552	9.8 (9.2 ± 0.4)
800	17.34	14.52	855	0.598	8.9 (8.2 ± 0.5)

[a]The average values of PCE are shown in the parentheses with the uncertainties representing one standard deviation.

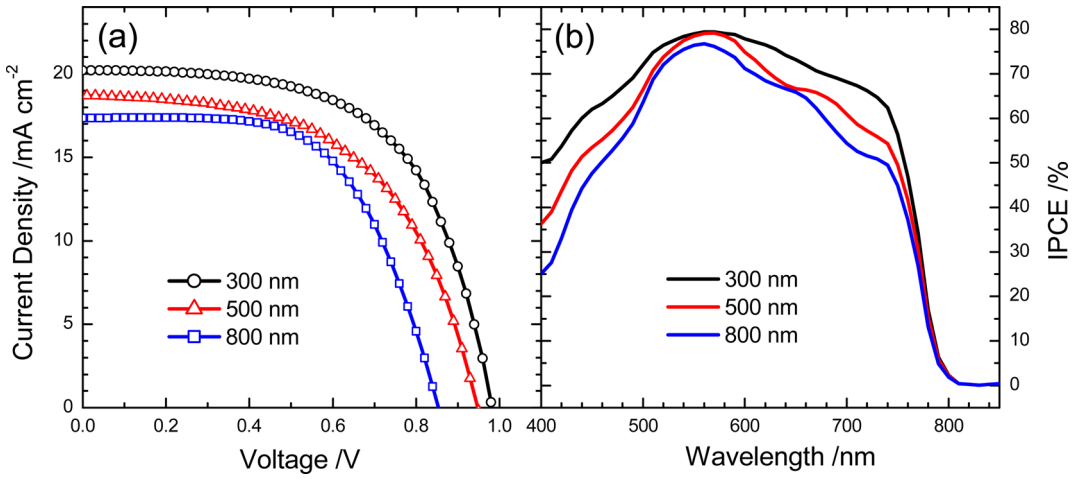

Figure 7. (a) Current–voltage curves and (b) IPCE spectra of perovskite solar cells with an om-TiO_2 layer of indicated thickness.

DOI: 10.1021/acs.jpcc.6b01980
J. Phys. Chem. C 2016, 120, 9619–9627

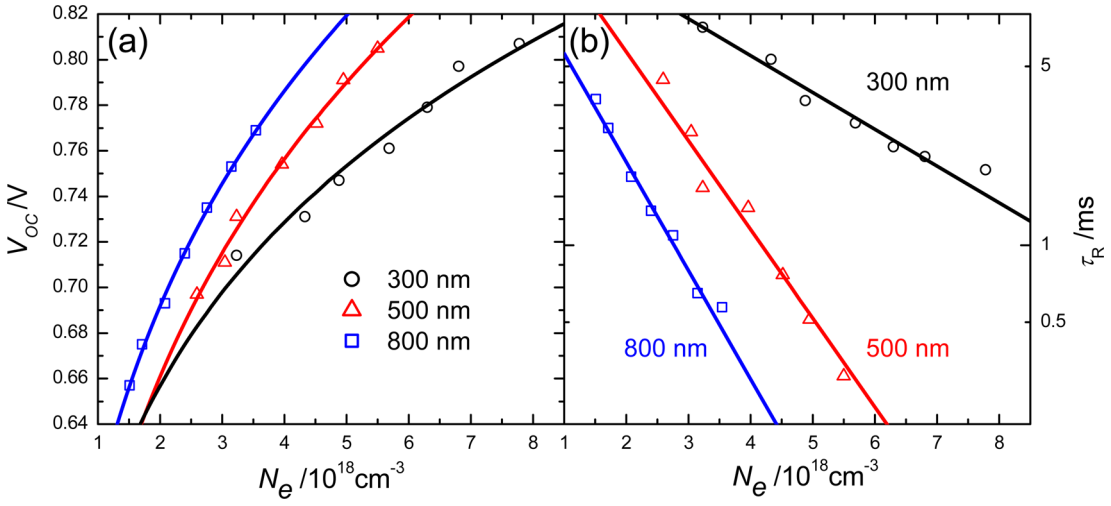

Figure 8. Plots of (a) V_{OC} as a function of charge density (N_e) and (b) charge recombination lifetime (τ_R) as a function of N_e for devices fabricated with om-TiO_2 layers of indicated thickness.

variation of the IPCE spectra, which display a decreased feature in regions both 400 and 700 nm upon increasing the film thickness. This phenomenon might be interpreted according to the penetration of illumination:[11] the generated charged carriers can be separated in a thin film more easily than in a thick film. For this reason, charge recombination might play a role to affect the values of V_{OC}. We thus made transient photoelectric measurements for the three tested devices using the charge extraction (CE) and transient photovoltage decays (TVD), as reported elsewhere.[56]

For the CE measurements, we used a white-light LED as a bias source to illuminate the devices under an open-circuit steady condition; the bias light was extinguished simultaneously with the system being switched to the short-circuit condition. The current transient under the latter condition was recorded and converted to a total charge density, N_e/cm^{-3}. Figure 8a shows plots of V_{OC} versus N_e at seven bias light intensities. The results indicate that, when compared at the same V_{OC} level, the charge densities extracted from om-TiO_2 show a trend with N_e (300 nm) > N_e (500 nm) > N_e (800 nm), implying that more charge carriers were produced in a thin film. This observation is consistent with the trend of J_{SC} (Table 1) which might be attributed to the limitation of charge collection associated with a relatively short diffusion length reported by Zhu and co-workers,[15] for which the mesoscopic perovskite devices were fabricated using conventional TiO_2 nanoparticles (NP). However, the best performance of conventional mesoscopic devices occurred at the TiO_2 film thickness 650 nm due to the insufficient perovskite loading at thinner films.[15] In our case, perovskite loading on the om-TiO_2 layer was not a problem so that the best performance of the om-TiO_2 devices was obtained at a much thinner film thickness (300 nm). Although an ordered mesoporous TiO_2 electrode may offer better transport characteristic than the conventional NP-based electrode, the extracted charges may not come from the TiO_2 layer exclusively. For example, Bisquert, Park, and their co-workers[57] pointed out that the photoinduced charges were accumulated inside the perovskite rather than the TiO_2 layer based on impedance spectral measurements. Our results are consistent with their conclusion because charge recombination might be more significant for the device fabricated with a thicker film thickness, for which we discuss in the following.

Greater charge densities might accelerate charge recombination at the open-circuit condition; we thus compared lifetime τ_R for charge recombination for all devices under the same N_e level. For the TVD measurements, we measured values of τ_R via transients induced with a second LED pulse under a bias irradiation at an open-circuit condition. Figure 8b shows plots of τ_R versus N_e at seven bias light intensities. According to the ambipolar properties of perovskite crystals, the generated charge carriers transport through the perovskite layer; charge recombination occurs at the perovskite/spiro-OMeTAD or perovskite/TiO_2 interface to decrease V_{OC}.[58] The larger τ_R implies a slower charge recombination at both interfaces and thus increases V_{OC}, consistent with the trend of V_{OC} showing the order V_{OC} (300 nm) > V_{OC} (500 nm) > V_{OC} (800 nm). Perovskite deposited on a thinner om-TiO_2 layer hence generated more charge carriers with slower charge recombination that gave superior device performance, as we observed.

CONCLUSION

We fabricated efficient solid-state mesoscopic perovskite solar cells based on organized mesoporous TiO_2 (om-TiO_2) layers with high porosity, larger pores and good interconnectivity, covered with perovskite crystals synthesized according to a sequential procedure with a prewetting treatment. This prewetting between the two steps decreased the residue of PbI_2 and increased the loading of perovskite crystals, which improved the device performance. The om-TiO_2 layers were formed with an inorganic sol–gel process using PVC-*g*-POEM graft copolymers of which the pore size and film thickness were controlled by varied hydrophobic PVC domains of the graft copolymers and varied precursor concentrations; the device fabricated with pore size 70 nm and film thickness 300 nm exhibited the best performance: J_{SC}/mA cm^{-2} = 20.21, V_{OC}/mV = 982, FF = 0.599, PCE = 11.9%. Measurements of charge extraction and transient photovoltage decay showed that more charge carriers were produced for the om-TiO_2 device of film thickness 300 nm than of 800 nm, consistent with the corresponding photovoltaic performance. The om-TiO_2 nanostructures are hence potential *n*-type electrode materials with an effective electron transport layer, enabling a fabrication of cost-effective and highly efficient mesoscopic perovskite solar cells.

DOI: 10.1021/acs.jpcc.6b01980
J. Phys. Chem. C 2016, 120, 9619–9627

■ ASSOCIATED CONTENT

Supporting Information

The Supporting Information is available free of charge on the ACS Publications website at DOI: 10.1021/acs.jpcc.6b01980.

Supplementary Figures S1−S6 and supplementary Tables S1−S5 (PDF).

■ AUTHOR INFORMATION

Corresponding Authors

*E-mail: diau@mail.nctu.edu.tw. Fax: +886-3-5723764. Tel.: +886-3-5131524.

*E-mail: jonghak@yonsei.ac.kr. Tel.: +82-2-2123-5757.

Author Contributions

‡These authors contributed equally to this work (C.-C.C. and C.S.L.).

Notes

The authors declare no competing financial interest.

■ ACKNOWLEDGMENTS

The Korea−Taiwan joint project supported this work under Contract Number MOST 103-2923-M-009-005-MY2.

■ REFERENCES

(1) Yang, W. S.; Noh, J. H.; Jeon, N. J.; Kim, Y. C.; Ryu, S.; Seo, J.; Seok, S. I. High-Performance Photovoltaic Perovskite Layers Fabricated Through Intramolecular Exchange. *Science* **2015**, *348*, 1234−1237.

(2) Ahn, N.; Son, D. Y.; Jang, I. H.; Kang, S. M.; Choi, M.; Park, N. G. Highly Reproducible Perovskite Solar Cells with Average Efficiency of 18.3% and Best Efficiency of 19.7% Fabricated via Lewis Base Adduct of Lead (II) Iodide. *J. Am. Chem. Soc.* **2015**, *137*, 8696−8699.

(3) Mei, A.; Li, X.; Liu, L.; Ku, Z.; Liu, T.; Rong, Y.; Xu, M.; Hu, M.; Chen, J.; Yang, Y.; Grätzel, M.; Han, H. A Hole-Conductor−Free, Fully Printable Mesoscopic Perovskite Solar Cell with High Stability. *Science* **2014**, *345*, 295−298.

(4) Lee, M. M.; Teuscher, J.; Miyasaka, T.; Murakami, T. N.; Snaith, H. J. Efficient Hybrid Solar Cells Based on Meso-Superstructured Organometal Halide Perovskites. *Science* **2012**, *338*, 643−647.

(5) Rhee, J. H.; Chung, C.-C.; Diau, E. W.-G. A Perspective of Mesoscopic Solar Cells Based on Metal Chalcogenide Quantum Dots and Organometal-Halide Perovskites. *NPG Asia Mater.* **2013**, *5*, e68.

(6) Kim, H. S.; Lee, C. R.; Im, J. H.; Lee, K. B.; Moehl, T.; Marchioro, A.; Moon, S. J.; Humphry-Baker, R.; Yum, J. H.; Moser, J. E.; Gratzel, M.; Park, N. G. Lead Iodide Perovskite Sensitized All-Solid-State Submicron Thin Film Mesoscopic Solar Cell with Efficiency Exceeding 9%. *Sci. Rep.* **2012**, *2*, 591−597.

(7) Li, M.-H.; Shen, P.-S.; Wang, K.-C.; Guo, T.-F.; Chen, P. Inorganic p-type Contact Materials for Perovskite-Based Solar Cells. *J. Mater. Chem. A* **2015**, *3*, 9011−9019.

(8) Salim, T.; Sun, S.; Abe, Y.; Krishna, A.; Grimsdale, A. C.; Lam, Y. M. Perovskite-Based Solar Cells: Impact of Morphology and Device Architecture on Device Performance. *J. Mater. Chem. A* **2015**, *3*, 8943−8969.

(9) Green, M. A.; Ho-Baillie, A.; Snaith, H. J. The Emergence of Perovskite Solar Cells. *Nat. Photonics* **2014**, *8*, 506−514.

(10) Jeon, N. J.; Noh, J. H.; Kim, Y. C.; Yang, W. S.; Ryu, S.; Seok, S. I. Solvent Engineering for High-Performance Inorganic−Organic Hybrid Perovskite Solar Cells. *Nat. Mater.* **2014**, *13*, 897−903.

(11) Wang, K.-C.; Jeng, J.-Y.; Shen, P.-S.; Chang, Y.-C.; Diau, E. W.-G.; Tsai, C.-H.; Chao, T.-Y.; Hsu, H.-C.; Lin, P.-Y.; Chen, P.; Guo, T.-F.; Wen, T.-C. p-type Mesoscopic Nickel Oxide/Organometallic Perovskite Heterojunction Solar Cells. *Sci. Rep.* **2014**, *4*, 4756−4763.

(12) Yang, Y.; Ri, K.; Mei, A.; Liu, L.; Hu, M.; Liu, T.; Li, X.; Han, H. The Size Effect of TiO_2 Nanoparticles on a Printable Mesoscopic Perovskite Solar Cell. *J. Mater. Chem. A* **2015**, *3*, 9103−9107.

(13) Aharon, S.; Gamliel, S.; Cohen, B. E.; Etgar, L. Depletion Region Effect of Highly Efficient Hole Conductor Free $CH_3NH_3PbI_3$ Perovskite Solar Cells. *Phys. Chem. Chem. Phys.* **2014**, *16*, 10512−10518.

(14) Kim, H. S.; Park, N. G. Parameters Affecting I−V Hysteresis of $CH_3NH_3PbI_3$ Perovskite Solar Cells: Effects of Perovskite Crystal Size and Mesoporous TiO_2 Layer. *J. Phys. Chem. Lett.* **2014**, *5*, 2927−2934.

(15) Zhao, Y.; Nardes, A. M.; Zhu, K. Solid-State Mesostructured Perovskite $CH_3NH_3PbI_3$ Solar Cells: Charge Transport, Recombination, and Diffusion Length. *J. Phys. Chem. Lett.* **2014**, *5*, 490−494.

(16) Lee, J. W.; Lee, T. Y.; Yoo, P. J.; Gratzel, M.; Mhaisalkar, S.; Park, N. G. Rutile TiO_2-Based Perovskite Solar Cells. *J. Mater. Chem. A* **2014**, *2*, 9251−9259.

(17) Im, J. H.; Jang, I. H.; Pellet, N.; Grätzel, M.; Park, N. G. Growth of $CH_3NH_3PbI_3$ Cuboids with Controlled Size for High-Efficiency Perovskite Solar Cells. *Nat. Nanotechnol.* **2014**, *9*, 927−932.

(18) Jeon, N. J.; Noh, J. H.; Yang, W. S.; Kim, Y. C.; Ryu, S.; Seo, J.; Seok, S. I. Compositional Engineering of Perovskite Materials for High-Performance Solar Cells. *Nature* **2015**, *517*, 476−480.

(19) Kim, H. S.; Im, S. H.; Park, N. G. Organolead Halide Perovskite: New Horizons in Solar Cell Research. *J. Phys. Chem. C* **2014**, *118*, 5615−5625.

(20) Murugadoss, G.; Mizuta, G.; Tanaka, S.; Nishino, H.; Umeyama, T.; Imahori, H.; Ito, S. Double Functions of Porous TiO_2 Electrodes on $CH_3NH_3PbI_3$ Perovskite Solar Cells: Enhancement of Perovskite Crystal Transformation and Prohibition of Short Circuiting. *APL Mater.* **2014**, *2*, 081511.

(21) Jiang, Q.; Sheng, X.; Li, Y.; Feng, X.; Xu, T. Rutile TiO_2 Nanowire-Based Perovskite Solar Cells. *Chem. Commun.* **2014**, *50*, 14720−14723.

(22) Qiu, J.; Qiu, Y.; Yan, K.; Zhong, M.; Mu, C.; Yan, H.; Yang, S. All-Solid-State Hybrid Solar Cells Based on a New Organometal Halide Perovskite Sensitizer and One-Dimensional TiO_2 Nanowire Arrays. *Nanoscale* **2013**, *5*, 3245−3248.

(23) Sung, S. D.; Ojha, D. P.; You, J. S.; Lee, J.; Kim, J.; Lee, W. I. 50 nm Sized Spherical TiO_2 Nanocrystals for Highly Efficient Mesoscopic Perovskite Solar Cells. *Nanoscale* **2015**, *7*, 8898−8906.

(24) Yang, I. S.; You, J. S.; Sung, S. D.; Chung, C. W.; Kim, J.; Lee, W. I. Novel Spherical TiO_2 Aggregates with Diameter of 100 nm for Efficient Mesoscopic Perovskite Solar Cells. *Nano Energy* **2016**, *20*, 272−282.

(25) Sarkar, A.; Jeon, N. J.; Noh, J. H.; Seok, S. I. Well-Organized Mesoporous TiO_2 Photoelectrodes by Block Copolymer-Induced Sol−Gel Assembly for Inorganic−Organic Hybrid Perovskite Solar Cells. *J. Phys. Chem. C* **2014**, *118*, 16688−16693.

(26) Feng, X.; Zhu, K.; Frank, A. J.; Grimes, C. A.; Mallouk, T. E. Rapid Charge Transport in Dye-Sensitized Solar Cells Made from Vertically Aligned Single-Crystal Rutile TiO_2 Nanowires. *Angew. Chem., Int. Ed.* **2012**, *51*, 2727−2730.

(27) Kim, H. S.; Lee, J. W.; Yantara, N.; Boix, P. P.; Kulkarni, S. A.; Mhaisalkar, S.; Grätzel, M.; Park, N. G. High Efficiency Solid-State Sensitized Solar Cell-Based on Submicrometer Rutile TiO_2 Nanorod and $CH_3NH_3PbI_3$ Perovskite Sensitizer. *Nano Lett.* **2013**, *13*, 2412−2417.

(28) Gao, X.; Li, J.; Baker, J.; Hou, Y.; Guan, D.; Chen, J.; Yuan, C. Enhanced Photovoltaic Performance of Perovskite $CH_3NH_3PbI_3$ Solar Cells with Freestanding TiO_2 Nanotube Array Films. *Chem. Commun.* **2014**, *50*, 6368−6371.

(29) Deng, Y.; Wei, J.; Sun, Z.; Zhao, D. Large-Pore Ordered Mesoporous Materials Templated from Non-Pluronic Amphiphilic Block Copolymers. *Chem. Soc. Rev.* **2013**, *42*, 4054−4070.

(30) Stefik, M.; Song, J.; Sai, H.; Guldin, S.; Boldrighini, P.; Orilall, M. C.; Steiner, U.; Gruner, S. M.; Wiesner, U. Ordered Mesoporous Titania from Highly Amphiphilic Block Copolymers: Tuned Solution Conditions Enable Highly Ordered Morphologies and Ultra-Large Mesopores. *J. Mater. Chem. A* **2015**, *3*, 11478−11492.

(31) Xu, D.; Yao, Y.; Han, L.; Che, S. Molecular Design of the Amphiphilic AB Diblock Copolymer Toward One-Step Synthesis of

DOI: 10.1021/acs.jpcc.6b01980
J. Phys. Chem. C 2016, 120, 9619−9627

Amino-Group Functionalized Large Pore Mesoporous Silica. *RSC Adv.* **2014**, *4*, 43047−43051.
(32) Xu, D.; Huang, Z.; Han, L.; Yao, Y.; Che, S. Amphiphilic ABC Triblock Terpolymer Templated Large-Pore Mesoporous Silicas. *Mater. Lett.* **2015**, *141*, 176−179.
(33) Gu, D.; Schuth, F. Synthesis of Non-Siliceous Mesoporous Oxides. *Chem. Soc. Rev.* **2014**, *43*, 313−344.
(34) Liu, B.; Luo, Z.; Federico, A.; Song, W.; Suib, S. L.; He, J. Colloidal Amphiphile-Templated Growth of Highly Crystalline Mesoporous Nonsiliceous Oxides. *Chem. Mater.* **2015**, *27*, 6173−6176.
(35) Xiong, Y.; He, D.; Jin, Y.; Cameron, P. J.; Edler, K. J. Ordered Mesoporous Particles in Titania Films with Hierarchical Structure as Scattering Layers in Dye-Sensitized Solar Cells. *J. Phys. Chem. C* **2015**, *119*, 22552−22559.
(36) Kim, H. J.; Jeon, J. D.; Chung, J. W.; Kwak, S. Y. Amplified Visible Light Photocatalytic Activity of Mesoporous TiO_2/ZnPc Hybrid by Cascade Mie Light Scattering. *Microporous Mesoporous Mater.* **2014**, *198*, 170−174.
(37) Kim, J. M.; Stucky, G. D. Synthesis of Highly Ordered Mesoporous Silica Materials Using Sodium Silicate and Amphiphilic Block Copolymers. *Chem. Commun.* **2000**, 1159−1160.
(38) Keshavarzi, R.; Mirkhani, V.; Moghadam, M.; Tangestaninejad, S.; Mohammadpoor-Baltork, I. Performance Enhancement of Dye-Sensitized Solar Cells Based on TiO_2 Thick Mesoporous Photoanodes by Morphological Manipulation. *Langmuir* **2015**, *31*, 11659−11670.
(39) Tan, K. W.; Moore, D. T.; Saliba, M.; Sai, H.; Estroff, L. A.; Hanrath, T.; Snaith, H. J.; Wiesner, U. Thermally Induced Structural Evolution and Performance of Mesoporous Block Copolymer-Directed Alumina Perovskite Solar Cells. *ACS Nano* **2014**, *8*, 4730−4739.
(40) Ahn, S. H.; Koh, J. H.; Seo, J. A.; Kim, J. H. Structure Control of Organized Mesoporous TiO_2 Films Templated by Graft Copolymers for Dye-Sensitized Solar Cells. *Chem. Commun.* **2010**, *46*, 1935−1937.
(41) Burschka, J.; Pellet, N.; Moon, S. J.; Humphry-Baker, R.; Gao, P.; Nazeeruddin, M. K.; Gratzel, M. Sequential Deposition as a Route to High-Performance Perovskite-Sensitized Solar Cells. *Nature* **2013**, *499*, 316−319.
(42) Roh, D. K.; Park, J. T.; Ahn, S. H.; Ahn, H.; Ryu, D. Y.; Kim, J. H. Amphiphilic Poly(vinyl chloride)-g-poly(oxyethylene methacrylate) Graft Polymer Electrolytes: Interactions, Nanostructures and Applications to Dye-Sensitized Solar Cells. *Electrochim. Acta* **2010**, *55*, 4976−4981.
(43) Ahn, S. H.; Chi, W. S.; Park, J. T.; Koh, J. K.; Roh, D. K.; Kim, J. H. Direct Assembly of Preformed Nanoparticles and Graft Copolymer for the Fabrication of Micrometer-Thick, Organized TiO_2 Films: High Efficiency Solid-State Dye-Sensitized Solar Cells. *Adv. Mater.* **2012**, *24*, 519−522.
(44) Burke, J. T. IR Spectroscopy or Hooke's Law at the Molecular Level - A Joint Freshman Physics-Chemistry Experience. *J. Chem. Educ.* **1997**, *74*, 1213.
(45) Park, J. T.; Roh, D. K.; Patel, R.; Kim, E.; Ryu, D. Y.; Kim, J. H. Preparation of TiO_2 Spheres with Hierarchical Pores via Grafting Polymerization and Sol-Gel Process for Dye-Sensitized Solar Cells. *J. Mater. Chem.* **2010**, *20*, 8521−8530.
(46) Ahn, S. H.; Seo, J. A.; Kim, J. H.; Ko, Y.; Hong, S. U. Synthesis and Gas Permeation Properties of Amphiphilic Graft Copolymer Membranes. *J. Membr. Sci.* **2009**, *345*, 128−133.
(47) Baikie, T.; Fang, Y.; Kadro, J. M.; Schreyer, M.; Wei, F.; Mhaisalkar, S. G.; Graetzel, M.; White, T. J. Synthesis and Crystal Chemistry of the Hybrid Perovskite $CH_3NH_3PbI_3$ for Solid-State Sensitised Solar Cell Applications. *J. Mater. Chem. A* **2013**, *1*, 5628−5641.
(48) Chen, Q.; Zhou, H.; Song, T. B.; Luo, S.; Hong, Z.; Duan, H. S.; Dou, L.; Liu, Y.; Yang, Y. Controllable Self-Induced Passivation of Hybrid Lead Iodide Perovskites toward High Performance Solar Cells. *Nano Lett.* **2014**, *14*, 4158−4163.
(49) Shiu, J.-W.; Lan, C.-M.; Chang, Y.-C.; Wu, H.-P.; Huang, W.-K.; Diau, E. W.-G. Size-Controlled Anatase Titania Single Crystals with Octahedron-Like Morphology for Dye-Sensitized Solar Cells. *ACS Nano* **2012**, *6*, 10862−10873.
(50) Xiao, M.; Huang, F.; Huang, W.; Dkhissi, Y.; Zhu, Y.; Etheridge, J.; Gray-Weale, A.; Bach, U.; Cheng, Y. B.; Spiccia, L. A fast deposition-crystallization procedure for highly efficient lead iodide perovskite thin-film solar cells. *Angew. Chem., Int. Ed.* **2014**, *53*, 9898−9903.
(51) Xiao, Z.; Dong, Q.; Bi, C.; Shao, Y.; Yuan, Y.; Huang, J. Solvent annealing of perovskite-induced crystal growth for photovoltaic-device efficiency enhancement. *Adv. Mater.* **2014**, *26*, 6503−6509.
(52) Liang, P.-W.; Liao, C.-Y.; Chueh, C.-C.; Zuo, F.; Williams, S. T.; Xin, X.-K.; Lin, J.; Jen, A. K. Y. Additive enhanced crystallization of solution-processed perovskite for highly efficient planar-heterojunction solar cells. *Adv. Mater.* **2014**, *26*, 3748−3754.
(53) Zuo, C.; Ding, L. An 80.11% FF record achieved for perovskite solar cells by using the NH_4Cl additive. *Nanoscale* **2014**, *6*, 9935−9938.
(54) Heo, J. H.; Han, H. J.; Kim, D.; Ahn, T. K.; Im, S. H. Hysteresis-less inverted $CH_3NH_3PbI_3$ planar perovskite hybrid solar cells with 18.1% power conversion efficiency. *Energy Environ. Sci.* **2015**, *8*, 1602−1608.
(55) In order to confirm the trend of photovoltaic performance on the film thickness of the om-TiO_2 layer, we have carried out the $J-V$ measurement for the device with om-TiO_2 of 150 nm thickness; the corresponding result is shown in Figure S6, SI. The PCE of this device attained only 6.1%. This poor efficiency might be due to the film morphology of om-TiO_2, which was not uniform at 150 nm.
(56) Li, L.-L.; Chang, Y.-C.; Wu, H.-P.; Diau, E. W.-G. Characterisation of Electron Transport and Charge Recombination Using Temporally Resolved and Frequency-Domain Techniques for Dye-Sensitised Solar Cells. *Int. Rev. Phys. Chem.* **2012**, *31*, 420−467.
(57) Kim, H.-S.; Mora-Sero, I.; Gonzalez-Pedro, V.; Fabregat-Santiago, F.; Juarez-Perez, E. J.; Park, N.-G.; Bisquert, J. Mechanism of Carrier Accumulation in Perovskite Thin-absorber Solar Cells. *Nat. Commun.* **2013**, *4*, 2242.
(58) Leijtens, T.; Lauber, B.; Eperon, G. E.; Stranks, S. D.; Snaith, H. J. The Importance of Perovskite Pore Filling in Organometal Mixed Halide Sensitized TiO_2-Based Solar Cells. *J. Phys. Chem. Lett.* **2014**, *5*, 1096−1102.

DOI: 10.1021/acs.jpcc.6b01980
J. Phys. Chem. C 2016, 120, 9619−9627